Article

Precessing jet nozzle connecting to a spinning black hole in M87

https://doi.org/10.1038/s41586-023-06479-6

Received: 24 February 2023

Accepted: 25 July 2023

Published online: 27 September 2023

Check for updates

Yuzhu Cui[1,2,3,4]✉, Kazuhiro Hada[3,4], Tomohisa Kawashima[5], Motoki Kino[4,6], Weikang Lin[7], Yosuke Mizuno[2,8,9], Hyunwook Ro[10,11], Mareki Honma[4,12], Kunwoo Yi[13], Jintao Yu[14], Jongho Park[10,15], Wu Jiang[16,17], Zhiqiang Shen[16,17], Evgeniya Kravchenko[44], Juan-Carlos Algaba[18], Xiaopeng Cheng[10], Ilje Cho[10,19], Gabriele Giovannini[20,21], Marcello Giroletti[21], Taehyun Jung[10,22], Ru-Sen Lu[16,17,23], Kotaro Niinuma[24,25], Junghwan Oh[26], Ken Ohsuga[27], Satoko Sawada-Satoh[28], Bong Won Sohn[10,11,22], Hiroyuki R. Takahashi[29], Mieko Takamura[4,12], Fumie Tazaki[30], Sascha Trippe[13,31], Kiyoaki Wajima[10,22], Kazunori Akiyama[32,33,34], Tao An[16], Keiichi Asada[15], Salvatore Buttaccio[21], Do-Young Byun[10,22], Lang Cui[17,35], Yoshiaki Hagiwara[36], Tomoya Hirota[3,4], Jeffrey Hodgson[37], Noriyuki Kawaguchi[4], Jae-Young Kim[23,38], Sang-Sung Lee[10,22], Jee Won Lee[10], Jeong Ae Lee[10], Giuseppe Maccaferri[21], Andrea Melis[39], Alexey Melnikov[40], Carlo Migoni[39], Se-Jin Oh[10], Koichiro Sugiyama[41], Xuezheng Wang[16], Yingkang Zhang[16], Zhong Chen[16,17], Ju-Yeon Hwang[10], Dong-Kyu Jung[10], Hyo-Ryoung Kim[10], Jeong-Sook Kim[10,42], Hideyuki Kobayashi[3], Bin Li[16,17], Guanghui Li[35], Xiaofei Li[35], Zhiyong Liu[35], Qinghui Liu[16,17], Xiang Liu[35], Chung-Sik Oh[10], Tomoaki Oyama[4], Duk-Gyoo Roh[10], Jinqing Wang[16,17], Na Wang[17,35], Shiqiang Wang[35], Bo Xia[16], Hao Yan[35], Jae-Hwan Yeom[10], Yoshinori Yonekura[43], Jianping Yuan[35], Hua Zhang[35], Rongbing Zhao[16,17] & Weiye Zhong[16,17]

The nearby radio galaxy M87 offers a unique opportunity to explore the connections between the central supermassive black hole and relativistic jets. Previous studies of the inner region of M87 revealed a wide opening angle for the jet originating near the black hole[1–4]. The Event Horizon Telescope resolved the central radio source and found an asymmetric ring structure consistent with expectations from general relativity[5]. With a baseline of 17 years of observations, there was a shift in the jet's transverse position, possibly arising from an 8- to 10-year quasi-periodicity[3]. However, the origin of this sideways shift remains unclear. Here we report an analysis of radio observations over 22 years that suggests a period of about 11 years for the variation in the position angle of the jet. We infer that we are seeing a spinning black hole that induces the Lense–Thirring precession of a misaligned accretion disk. Similar jet precession may commonly occur in other active galactic nuclei but has been challenging to detect owing to the small magnitude and long period of the variation.

To accurately trace the long-term morphological evolution of the M87 jet near the supermassive black hole (SMBH), we analysed 170 very long baseline interferometry (VLBI) images of the M87 jet obtained with the East Asian VLBI Network (EAVN[6]) and the Very Long Baseline Array (VLBA[3]) at Q and K bands (referring to 43 GHz and 22–24 GHz, respectively) between 2000 and 2022 (Extended Data Figs. 1 and 2). Part of the EAVN observations at the K band was further connected to the telescopes in Italy and Russia (EATING[7]). The detailed information of the data and the joined antenna are listed in Extended Data Tables 1 and 2. Figure 1 presents a sequence of biyearly stacked EAVN and VLBA Q-band images obtained from 2013 to 2020. In addition to the well-known persistent limb-brightened jet morphology[8], one can see that the overall position angle (PA) of the jet direction near the core noticeably changes over the years.

Figure 2a displays the time evolution of the jet central PA averaged over distances of 0.7–3.0 milli-arcseconds (mas) measured for 164 individual epochs after excluding six epochs with poor quality (Methods). Although the error bars of individual data points are relatively large, the ensemble of 164 measurements clearly reveals a systematic year-scale oscillation of the jet PA with a peak-to-peak amplitude of approximately 10° centred at PA ≈ 288°. Note that the parsec-scale jet of M87 is known to exhibit short-term (weekly and monthly) structural variations for various reasons, such as: (1) episodic ejections of new jet components[9]; (2) bulk flow acceleration along the jet[10]; and (3) hydrodynamical instabilities that make the jet fluctuated transversely[11]. In addition, in combination with inhomogeneous image dynamic ranges among different epochs, these temporal effects cause large scatters in the measured PA among individual epochs within the same year. Hence, to smooth out short-term (less than 1-year-scale) temporal fluctuations and then highlight the long-term global systematic evolution of the jet base, we produced a sequence of yearly binned images by averaging multiple images over every single year. As shown in Fig. 2b, the yearly binned evolution of the jet PA obtained from the stacked images displays clear quasi-sinusoidal variations as a function of observing year t.

To characterize the periodic oscillation of the jet nozzle on the sky plane, we introduce a simple model of the precessing solid-body cone in

A list of affiliations appears at the end of the paper.

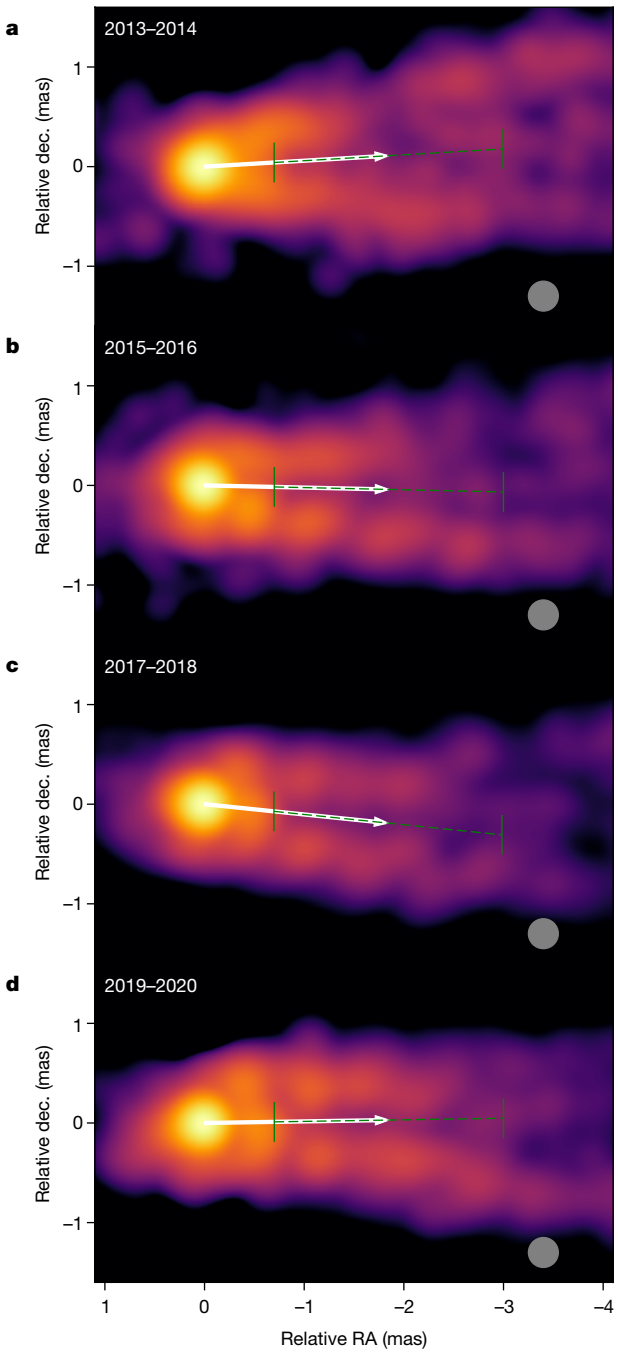

Fig. 1 | Structural evolution of M87 jet from 2013 to 2020. a–d, The images are produced by stacking individual EAVN and VLBA Q-band images over every two years. The nearby years are indicated at the top left-hand corner: 2013–2014 (**a**); 2015–2016 (**b**); 2017–2018 (**c**); 2019–2020 (**d**). The grey-coloured circle at the bottom right-hand corner of each panel indicates a common circular Gaussian beam with a full-width at half-maximum of 0.3 mas. All images are rotated by −18°. The white arrow in each panel indicates the jet PA averaged over a jet portion of 0.7–3.0 mas from the core (indicated by the green dotted line) in the corresponding stacked images. For M87, BH mass $M_{BH} = 6.5 \times 10\, M_{\odot}$ (ref. 5), 1 mas ≈ 250 r_g ≈ 0.08 pc. Dec., declination; RA, right ascension.

the three-dimensional space (Fig. 2c). The observed jet PA is identified as the angle of the jet axis projected on the sky, η, which is related to the intrinsic properties of the jet precession by applying a sequence of rotation matrices from the jet to the observer frame[12] (Methods). We note that the angular velocity of precession is expected to be non-relativistic and the jet portion considered in the present analysis (0.7–3.0 mas corresponding to the de-projected distances around 600–2,500 r_g for a viewing angle $\theta = 17.2°$ (ref. 3), where $r_g = GM_{BH}/c^2$ is the gravitational radius, M_{BH} is the black hole (BH) mass, G is the gravitational constant and c is the speed of light) is in the weak gravity region. Therefore, the effect of relativistic time dilation is considered to be negligible in our present modelling. We perform a likelihood analysis using the Markov chain Monte Carlo (MCMC) algorithm to a time series of the jet PA obtained from the yearly binned jet images between 2006 to 2022. The best fitting result of η is shown in Fig. 2b with a red thick line. The results of each parameter are listed in Table 1.

The long-term PA data are well matched by the jet precession model with a best-fit reduced chi-squared value $\hat{\chi}^2$ of 1.2. Note that two cycles are still not definitive to conclude a periodicity considering the possible effect of red noise. Nevertheless, the good agreement between the observations and the jet precession model and the putative periodicity of the jet PA variation cast doubts on alternative scenarios such as temporal oscillations by instabilities[3,13,14] (see more in Methods). In our fiducial analysis, we include some prior of the viewing angle ϕ to break the degeneracy between the half-opening angle ψ_{jet} of the jet precession cone and the angle θ between the precession axis and the line of sight, resulting in $\psi_{jet} = (1.25 \pm 0.18)°$. The deduced $|\omega_p| = (0.56 \pm 0.02)$ radians per year corresponds to a precession period of $T_{prec}^{jet} = (11.24 \pm 0.47)$ years, which is comparable to the 8–10 year quasi-periodicity reported in ref. 3. The periodicity of the PA variation is robust regardless of whether we include the prior of ϕ, whether we only use a subset of data (that at Q band) and whether we include the earlier data (from 2000 to 2004) with poor quality (Methods, Extended Data Fig. 3 and Extended Data Tables 3–5). As the jet precesses, the mean value of the jet viewing angle ϕ oscillates between 16° and 18.5° with an uncertainty of approximately 2° each year. The inferred evolution of ϕ is shown in Extended Data Fig. 4 and its values for some selected years are listed in Extended Data Table 6.

The observed periodic PA variation in the M87 jet is likely to be triggered by certain physical and steady processes, and Lense–Thirring (LT) precession of a tilted accretion disk with respect to the SMBH spin[15] is a promising origin. In fact, since the matter accreting onto the SMBH is insensitive to the BH spin direction, a certain misalignment between the angular momentum vector of the accretion disk and that of the SMBH spin is expected to commonly exist in active galactic nuclei with the level of misalignment depending on how exactly the SMBH became part of the system[16,17]. This configuration can generate LT precession of the accretion disk caused by the frame-dragging force of a spinning BH[15], which is expected to propagate to the jet through the tight coupling between the jet and the accretion disk[17,18].

Extensive general relativistic magnetohydrodynamics (GRMHD) simulations exploring misaligned systems have demonstrated that the majority of the accretion disk coherently experiences LT precession[16,18–21] and that the jet, indeed, precesses in phase with the disk[17,18]. Adopting the SMBH mass of M87, the pioneering work by refs. 16,19 reproduced a precession period of the same order of magnitude as that deduced in this work. Here, we further develop and conduct our GRMHD simulations with settings closely resembling the M87 system and successfully recover the disk and jet precession in a tilted-disk-BH system over almost two cycles by using UWABAMI code[22,23] (Fig. 3 and Methods). A steady precession with a period consistent with the observations is revealed after the simulation converges at around $t = 16$ years, as indicated in Fig. 3b. Although we assume a spin parameter $a_* = 0.9375$, the exact relationship between the precession period and the BH spin is sensitive to the morphology of the disk[16,24].

The presence of LT precession indicates that the M87 central SMBH is spinning, which is essential for producing an energetic jet via the Blandford–Znajek mechanism[25]. However, the magnitude of spin is sensitive to the size of the disk according to $T_{prec} = \pi c^3 r_{LT}^3/(G^2 a_* M_{BH}^2)$ in the weak-field limit[16,26,27]. On the other hand, the effective radius is $r_{LT} \approx 15\, r_g$ for a maximally spinning SMBH, which suggests a compact

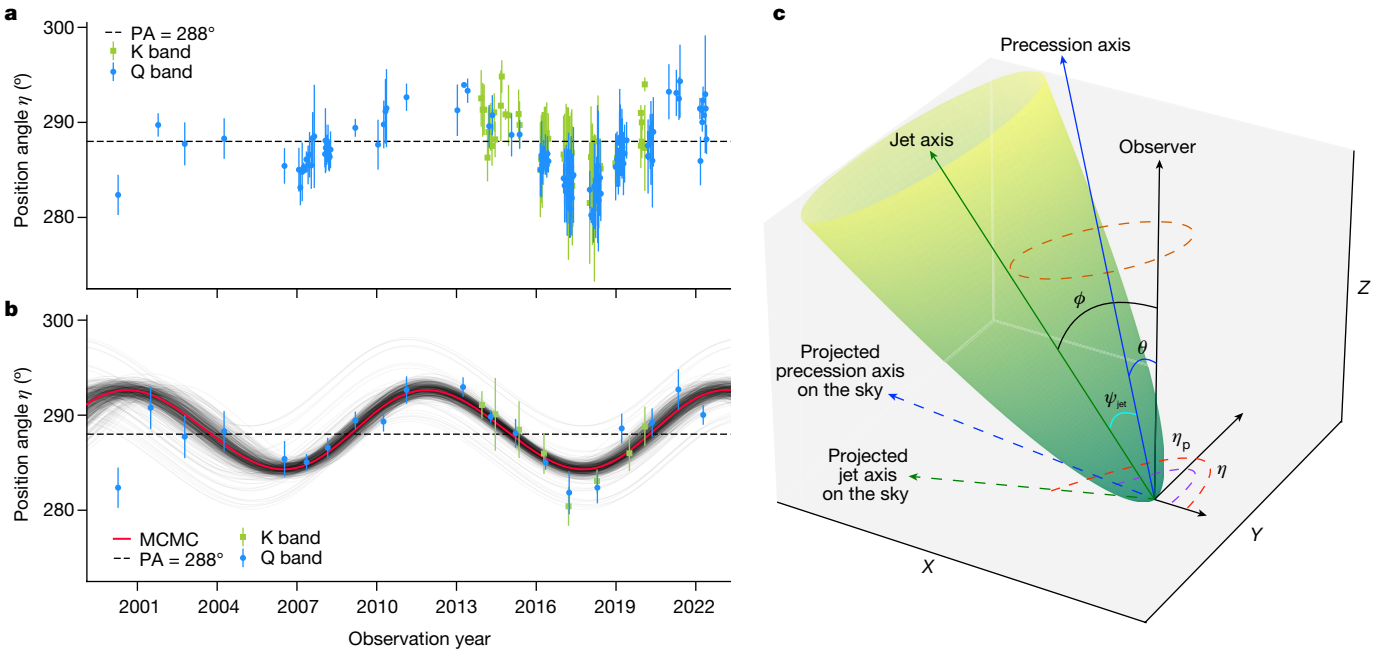

Fig. 2 | Time dependence of the M87 jet PA from 2000 to 2022 and a schematic picture of the precession model. a,**b**, Error bars represent the standard deviation derived from the Gaussian fitting. The green (blue) data points in **a** and **b** indicate the measured PA at K (Q) band. The horizontal dashed line represents the well-known jet PA in previous studies of M87 (ref. 3) in **a** and the best fit of η_p in **b**. For **a**, measurements were conducted with 164 individual epochs within the jet distances 0.7–3.0 mas (EAVN and VLBA Q band, EATING and VLBA K band) and 1.7–3.0 mas (EAVN K band). For **b**, the results were obtained from the yearly binned images with all 170 epochs. Owing to the stacking procedure according to the observing frequency, the measured region for EATING and VLBA K band data is within 1.7–3.0 mas core separation (Methods). The red line is derived from the best-fit precession model parameters (Table 1). The thin grey lines represent the statistical errors, which are randomly chosen from the MCMC samples. **c**, (X,Y) is the sky plane. As the jet precesses, the central axis (solid green arrow) of the parabolic jet (green surface) rotates with respect to the precession axis (solid blue arrow) along the trajectory indicated by the dotted orange circle. The surface traced out by the jet's central axis is dubbed the 'precession cone'. The dotted blue (green) arrow represents the projected precession (jet) axis. The PA of the projected jet axis η (red dotted arc), the PA of the projected precession axis η_p (purple dotted arc), the half-opening angle of the jet precession cone ψ_{jet} (cyan arc) and the angle between the line of sight (Z axis) and the jet (precession) axis ϕ (θ) are labelled accordingly.

disk region that undergoes coherent LT precession and motivates us to adopt a small disk in simulations. The small value of ψ_{jet} implies a small misalignment between the M87 jet at mas scales and the SMBH spin. Owing to the tight relationship between the jet and accretion disk[17,18], this further suggests a slight tilt of the accretion disk with respect to the SMBH spin. Such a configuration may naturally arise if the M87 central SMBH grew mainly through accretion[28,29]. However, the disk could have a finite tilt angle as the disk orientation can vary with radius[18,19]. In that case, since the bright side of the ring-like structure detected by the Event Horizon Telescope at 230 GHz can be connected to the relativistic jet base or (and) inner disk, the PA change of it[30] may synchronize with the PA change seen in the mas-scale jet. The recent Global Millimeter VLBI Array observations at 86 GHz, which successfully detected both the ring-like structure and jet, well fill the spatial gaps between mas and micro-arcsecond scales[4]. Further accumulating multi-year, multi-wavelength VLBI images are crucial to seamlessly connect the dynamic evolution of the structure from the emission surrounding the BH to the launching jet[20].

Table 1 | Summary of the parameters in the precession model

Parameter	Definition	Value	Unit
t_0	Reference time	2014.82±0.15	year
η_p	PA of the precession axis	288.47±0.27	degrees
$\lvert\omega_p\rvert$	Angular velocity of precession	0.56±0.02	radians per year
ψ_{jet}	Half-opening angle of the precession cone	1.25±0.18	degrees
θ	Angle between the precession axis and line of sight	17.21±1.74	degrees

The configuration of these free parameters refers to Fig. 2c. The values correspond to the means of the MCMC samples with standard deviations. The period of precession, $T^{jet}_{prec} = 2\pi/\omega_p = (11.24 \pm 0.47)$ years. The sense of precession (the sign of ω_p) cannot be determined by the observed PA of the jet axis η in this work.

Online content

Any methods, additional references, Nature Portfolio reporting summaries, source data, extended data, supplementary information, acknowledgements, peer review information; details of author contributions and competing interests; and statements of data and code availability are available at https://doi.org/10.1038/s41586-023-06479-6.

1. Junor, W., Biretta, J. A. & Livio, M. Formation of the radio jet in M87 at 100 Schwarzschild radii from the central black hole. *Nature* **401**, 891–892 (1999).
2. Hada, K. et al. An origin of the radio jet in M87 at the location of the central black hole. *Nature* **477**, 185–187 (2011).
3. Walker, R. C., Hardee, P. E., Davies, F. B., Ly, C. & Junor, W. The structure and dynamics of the subparsec jet in M87 based on 50 VLBA observations over 17 years at 43 GHz. *Astrophys. J.* **855**, 128 (2018).
4. Lu, R. et al. A ring-like accretion structure in M87 connecting its black hole and jet. *Nature* **616**, 686–690 (2023).
5. Event Horizon Telescope Collaboration. First M87 Event Horizon Telescope results. I. The shadow of the supermassive black hole. *Astrophys. J. Lett.* **875**, L1 (2019).
6. Cui, Y. Z. et al. East Asian VLBI Network observations of active galactic nuclei jets: imaging with KaVA+Tianma+Nanshan. *Res. Astron. Astrophys.* **21**, 205 (2021).
7. Giovannini, G. et al. The past and future of East Asia to Italy: nearly global VLBI. *Galaxies* **11**, 49 (2023).

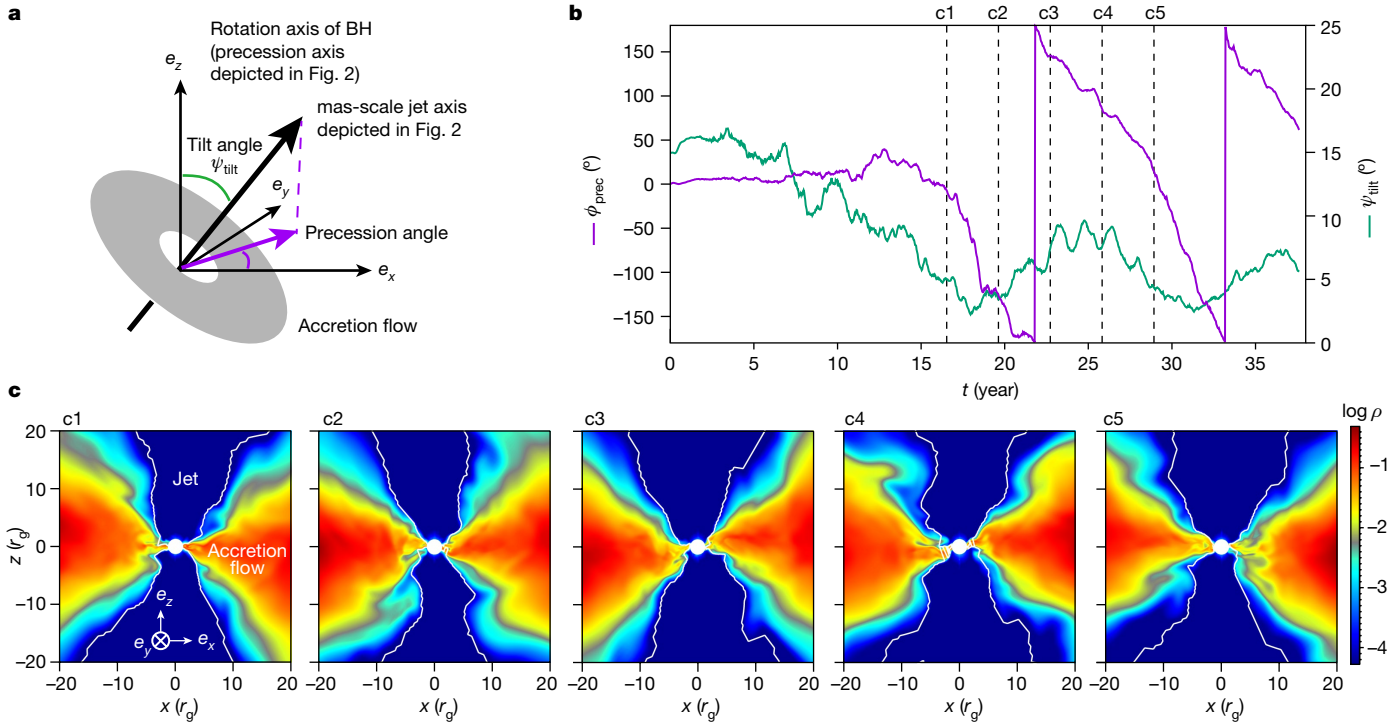

Fig. 3 | GRMHD simulation. a, Configuration of the BH spin axis and mas-scale jet axis. $\psi_{\rm tilt}$ is the tilt angle of the mas-scale jet axis with respect to the BH spin axis (z axis). $\phi_{\rm prec}$ is the projected angle of the mas-scale jet axis relative to the x axis, which traces the precession of accretion flow. Here, the mas-scale jet axis is almost aligned with the rotation axis of the accretion flow and slow outflow due to the collimation effect while the jet axis is aligned with the BH spin axis near the event horizon[17,18]. **b**, Evolution of $\psi_{\rm tilt}$ and $\phi_{\rm prec}$ as a function of time evaluated at $r = 20\,r_{\rm g}$. Five time points, $t_1 = 16.23$ years (c1), $t_2 = 19.27$ years (c2), $t_3 = 22.32$ years (c3), $t_4 = 25.36$ years (c4) and $t_5 = 28.41$ years (c5) are indicated with dashed lines. **c**, Snapshots of mass density ρ of the GRMHD simulation results corresponding to the five time points indicated in **b**, where ρ is measured in the fluid-rest frame. We set $M_{\rm BH} = 6.5 \times 10^9 M_\odot$ for the conversion of the time unit in the GRMHD simulation $r_{\rm g}/c$ to year. The total simulated time is $3.7 \times 10\,r_{\rm g}/c$, namely, 37.5 years. We take a spin parameter $a_* = 0.9375$. The white contours depict the surface of magnetization $\sigma(\equiv B^2/\rho c^2) = 1$, where B is the magnetic field strength in the fluid-rest frame. We define the regions $\sigma > 1$ (that is, the region near the z axis inside the contour) as the relativistic jets.

8. Hada, K. et al. High-sensitivity 86 GHz (3.5 mm) VLBI observations of M87: deep imaging of the jet base at a resolution of 10 Schwarzschild radii. *Astrophys. J.* **817**, 131 (2016).
9. Hada, K. et al. A strong radio brightening at the jet base of M87 during the elevated very high energy gamma-ray state in 2012. *Astrophys. J.* **788**, 165 (2014).
10. Park, J. et al. Kinematics of the M87 jet in the collimation zone: gradual acceleration and velocity stratification. *Astrophys. J.* **887**, 147 (2019).
11. Ro, H. et al. Transverse oscillations of the M87 jet revealed by KaVA observations. *Galaxies* **11**, 33 (2023).
12. Caproni, A. & Abraham, Z. Precession in the inner jet of 3C 345. *Astrophys. J.* **602**, 625–634 (2004).
13. Mizuno, Y., Hardee, P. & Nishikawa, K. I. Three-dimensional relativistic magnetohydrodynamic simulations of magnetized spine-sheath relativistic jets. *Astrophys. J.* **662**, 835–850 (2007).
14. Mizuno, Y., Lyubarsky, Y., Nishikawa, K. I. & Hardee, P. E. Three-dimensional relativistic magnetohydrodynamic simulations of current-driven instability. III. Rotating relativistic jets. *Astrophys. J.* **757**, 16 (2012).
15. Lense, J. & Thirring, H. *Über den Einfluß der Eigenrotation der Zentralkörper auf die Bewegung der Planeten und Monde nach der Einsteinschen Gravitationstheorie. Physikalische Zeitschrift* **19**, 156–163 (1918).
16. Fragile, P. C., Blaes, O. M., Anninos, P. & Salmonson, J. D. Global general relativistic magnetohydrodynamic simulation of a tilted black hole accretion disk. *Astrophys. J.* **668**, 417–429 (2007).
17. McKinney, J. C., Tchekhovskoy, A. & Blandford, R. D. Alignment of magnetized accretion disks and relativistic jets with spinning black holes. *Science* **339**, 49–52 (2013).
18. Liska, M. et al. Formation of precessing jets by tilted black hole discs in 3D general relativistic MHD simulations. *Mon. Not. R. Astron. Soc.* **474**, L81–L85 (2018).
19. White, C. J., Quataert, E. & Blaes, O. Tilted disks around black holes: a numerical parameter survey for spin and inclination angle. *Astrophys. J.* **878**, 51 (2019).
20. Chatterjee, K. et al. Observational signatures of disc and jet misalignment in images of accreting black holes. *Mon. Not. R. Astron. Soc.* **499**, 362–378 (2020).
21. Ressler, S. M., White, C. J. & Quataert, E. Wind-fed GRMHD simulations of Sagittarius A*: tilt and alignment of jets and accretion discs, electron thermodynamics, and multiscale modelling of the rotation measure. *Mon. Not. R. Astron. Soc.* **521**, 4277–4298 (2023).
22. Takahashi, H. R., Ohsuga, K., Kawashima, T. & Sekiguchi, Y. Formation of overheated regions and truncated disks around black holes: three-dimensional general relativistic radiation-magnetohydrodynamics simulations. *Astrophys. J.* **826**, 23 (2016).
23. Kawashima, T., Ohsuga, K. & Takahashi, H. R. RAIKOU: a general relativistic, multiwavelength radiative transfer code. *Astrophys. J.* **949**, 101 (2023).
24. Liu, S. & Melia, F. An accretion-induced X-ray flare in Sagittarius A*. *Astrophys. J. Lett.* **566**, L77–L80 (2002).
25. Blandford, R. D. & Znajek, R. L. Electromagnetic extraction of energy from Kerr black holes. *Mon. Not. R. Astron. Soc.* **179**, 433–456 (1977).
26. Wilkins, D. C. Bound geodesics in the Kerr metric. *Phys. Rev. D* **5**, 814–822 (1972).
27. Caproni, A., Abraham, Z., Livio, M. & Mosquera Cuesta, H. J. Is the Bardeen–Petterson effect responsible for the warping and precession in NGC4258? *Mon. Not. R. Astron. Soc.* **379**, 135–142 (2007).
28. Scheuer, P. A. G. & Feiler, R. The realignment of a black hole misaligned with its accretion disc. *Mon. Not. R. Astron. Soc.* **282**, 291–294 (1996).
29. Natarajan, P. & Armitage, P. J. Warped discs and the directional stability of jets in active galactic nuclei. *Mon. Not. R. Astron. Soc.* **309**, 961–968 (1999).
30. Wielgus, M. & Event Horizon Telescope Collaboration. Monitoring the morphology of M87* in 2009–2017 with the Event Horizon Telescope. *Astrophys. J.* **901**, 67 (2020).

[1]Research Center for Intelligent Computing Platforms, Zhejiang Laboratory, Hangzhou, China. [2]Tsung-Dao Lee Institute, Shanghai Jiao Tong University, Shanghai, China. [3]Astronomical Science Program, The Graduate University for Advanced Studies, Mitaka, Japan. [4]Mizusawa VLBI Observatory, National Astronomical Observatory of Japan, Oshu, Japan. [5]Institute for Cosmic Ray Research, The University of Tokyo, Kashiwa, Japan. [6]Kogakuin University of Technology & Engineering, Academic Support Center, Hachioji, Japan. [7]South-Western Institute For Astronomy Research, Yunnan University, Kunming, China. [8]School of Physics and Astronomy, Shanghai Jiao Tong University, Shanghai, China. [9]Institut für Theoretische Physik, Goethe-Universität Frankfurt, Frankfurt, Germany. [10]Korea Astronomy and Space Science

Institute, Daejeon, Republic of Korea. [11]Department of Astronomy, Yonsei University, Seodaemun-gu, Republic of Korea. [12]Department of Astronomy, Graduate School of Science, The University of Tokyo, Bunkyo, Japan. [13]Department of Physics and Astronomy, Seoul National University, Gwanak-gu, Republic of Korea. [14]Department of Intelligence, Air Force Early Warning Academy, Wuhan, China. [15]Institute of Astronomy and Astrophysics, Academia Sinica, Hilo, HI, USA. [16]Shanghai Astronomical Observatory, Chinese Academy of Sciences, Shanghai, China. [17]Key Laboratory of Radio Astronomy and Technology, Chinese Academy of Sciences, Beijing, China. [18]Department of Physics, Faculty of Science, Universiti Malaya, Kuala Lumpur, Malaysia. [19]Instituto de Astrofísica de Andalucía - CSIC, Glorieta de la Astronomía s/n, Granada, Spain. [20]DIFA Bologna University, Bologna, Italy. [21]INAF-Istituto di Radioastronomia, Bologna, Italy. [22]University of Science and Technology, Yuseong-gu, Republic of Korea. [23]Max-Planck-Institut für Radioastronomie, Bonn, Germany. [24]Graduate School of Sciences and Technology for Innovation, Yamaguchi University, Yamaguchi, Japan. [25]The Research Institute for Time Studies, Yamaguchi University, Yamaguchi, Japan. [26]Joint Institute for VLBI ERIC, Dwingeloo, the Netherlands. [27]Center for Computational Sciences, University of Tsukuba, Tsukuba, Japan. [28]Graduate School of Science, Osaka Metropolitan University, Sakai, Japan. [29]Department of Natural Sciences, Faculty of Arts and Sciences, Komazawa University, Setagaya, Japan. [30]Tokyo Electron Technology Solutions Limited, Oshu City, Japan. [31]SNU Astronomy Research Center, Seoul National University, Gwanak-gu, Republic of Korea. [32]National Radio Astronomy Observatory, Charlottesville, VA, USA. [33]Massachusetts Institute of Technology Haystack Observatory, Westford, MA, USA. [34]Black Hole Initiative at Harvard University, Cambridge, MA, USA. [35]Xinjiang Astronomical Observatory, Chinese Academy of Sciences, Urumqi, China. [36]Toyo University, Bunkyo-ku, Japan. [37]Department of Physics and Astronomy, Sejong University, Gwangjin-gu, Republic of Korea. [38]Department of Astronomy and Atmospheric Sciences, Kyungpook National University, Daegu, Republic of Korea. [39]INAF - Osservatorio Astronomico di Cagliari, Selargius, CA, Italy. [40]Institute of Applied Astronomy, Russian Academy of Sciences, St. Petersburg, Russia. [41]National Astronomical Research Institute of Thailand (Public Organization), Chiangmai, Thailand. [42]National Astronomical Observatories, Chinese Academy of Sciences, Beijing, China. [43]Center for Astronomy, Ibaraki University, Mito, Japan. [44]Unaffiliated: Evgeniya Kravchenko. ✉e-mail: yuzhu_cui77@163.com

Methods

In what follows, we describe the methods and assumptions employed to derive our results in the main text.

Summary of observations and data

The data presented in this work are taken from EAVN and VLBA at 22, 24 and 43 GHz, and EATING (a joint array of EAVN and radio telescopes in Italy and Russia) at 22 GHz. The primary data among them are the ones obtained with EAVN and VLBA at 43 GHz, since these data provide finer angular resolution, imaging sensitivity and observing cadences to monitor the jet base, whereas the other data further complement the 43 GHz data (that is, higher resolution with EATING; larger field-of-view at 22 GHz). In total, the VLBI data we used for imaging analysis include 119 epochs from EAVN, 4 epochs from EATING and 47 epochs from VLBA. Basic information on the data from each of these VLBI arrays is summarized in Extended Data Table 1. Divided by observing frequency, there are 56 epochs at 22 or 24 GHz and 114 epochs at 43 GHz. The total observation period covered by these observations is from April 2000 to May 2022. All the individual data are summarized in Supplementary Information.

Notes on EAVN and EATING data

Since 2013, we have been regularly monitoring the pc-scale jet of M87 with EAVN, which is a joint VLBI network in East Asia. In each year, the EAVN monitoring observations were performed mainly from December to June with sampling intervals ranging from a few days to a month. Although the EAVN observations until 2016 were conducted with a joint array of KVN (Korean VLBI Network, Korea) and VERA (VLBI Exploration of Radio Astrometry, Japan), namely KaVA, from 2017, more stations in East Asia joined the network, enhancing the overall array performance. The angular resolution of only KaVA is 1.26 mas at 22 GHz and 0.63 mas at 43 GHz. The default array configurations from 2017 were KaVA + Tianma + Nanshan at 22 GHz and KaVA + Tianma at 43 GHz, respectively. This achieves a maximum angular resolution of 0.55 mas at 22 GHz and 0.63 mas at 43 GHz. Additionally, part of our EAVN 22 GHz observations were further connected to the telescopes in Italy (Medicina and Sardinia stations) or Russia (Badary station). We call this global network an 'EATING VLBI array' and extend our maximum baseline lengths from 5,078 km to approximately 10,000 km, resolving the regions closer to the BH at a resolution down to 0.27 mas (mainly in the east–west direction). We performed four epochs of EATING VLBI sessions between 2017 and 2020 (see Extended Data Table 2 for details).

Each of the EAVN and EATING sessions was made in a 5–7-hour continuous run at a data recording rate of 1 Gbps (a total bandwidth of 256 MHz). Only left-hand circular polarization was recorded. All the data were correlated at the Daejeon hardware correlator installed at Korea Astronomy and Space Science Institute. The correlated data were calibrated in the standard manner of VLBI data reduction procedures and under the guideline of EAVN data reduction[31]. The initial calibration of visibility amplitude, phase and bandpass was performed with the AIPS software package[32]. The subsequent imaging[33] and self-calibration were performed with the Difmap software[34].

Notes on VLBA archival data

To expand the time coverage of our study, we additionally reanalysed VLBA archival data obtained between 2000 and 2020. The VLBA data between 2006 and 2018 were part of a dedicated M87 monitoring program[3], whereas the data before 2006 were sparsely sampled with relatively lower imaging quality. There are three sessions observed at 24 GHz and 44 sessions observed at 43 GHz. The recording rate ranges from 128 Mbps to 2,048 Mbps depending on the sessions. Both left and right circular polarizations were recorded for most of these sessions. More detailed information for individual epochs can be found in refs. 3,35,36. The data reduction process follows the standard process of VLBA data reduction. After the phase and amplitude calibration in the AIPS software package, we did self-calibration and final imaging in the Difmap software. The angular resolution of the VLBA image was around 0.40 mas at 24 GHz and 0.23 mas at 43 GHz, respectively.

Measurement of jet position angle

We quantified the jet PA of M87 near the core in the following procedures. First, to reduce the effects from the shape of beam sizes, all images for the individual epochs were restored with a circular beam with sizes of 0.3 mas for VLBA-43GHz and EATING-22 GHz, 0.5 mas for EAVN-43 GHz and VLBA-24 GHz data and 1.2 mas for EAVN-22 GHz data. For each image, we then made circular slices (centred on the core) of the jet every 0.1 mas from $r_{\rm start}$ (the starting distance of slicing) to 3.0 mas along the jet and integrated them over all sliced distances. Here, $r_{\rm start}$ was set to at least 1.4 times the beam size of each image (0.7 mas for VLBA-43 GHz, EATING-22 GHz, VLBA-24 GHz, and EAVN-43 GHz images, and 1.7 mas for EAVN-22 GHz images) so that we could avoid the influences from the bright core[37]. The integration over a certain distance improved the significance and reduced the weight of the temporal emission caused by hydrodynamical instabilities in individual epochs. Then the integrated slice for each epoch was fitted with two or three Gaussian components owing to the well-known double-ridge or triple-ridge mas-scale jet profile of M87 (refs. 8,38). Finally, we defined the middle of the outer two Gaussian peaks as the central PA of the M87 jet for each epoch. The errors come from two parts: (1) image noise, which could be ignored owing to the high enough significance after integration within the innermost region; and (2) Gaussian fitting errors output from the program. As a result, we adopted the Gaussian fitting errors as the error bars in Fig. 2a,b. Note that the core shift between 22/24 GHz and 43 GHz was approximately 0.03 mas according to ref. 2, which is negligible when we determine the PA in Fig. 2a,b. Through these procedures, we obtained the PA (and its uncertainty) for the innermost region 0.7–3.0 mas in 164 individual epochs, as shown in Fig. 2a. Note that there are six epochs excluded in this individual epoch analysis owing to the poor data quality, as marked with * in Supplementary Information, which may have led to some apparent differences between individual and stacked analysis, such as the data point in 2001 shown in Fig. 2a,b.

In addition to the above-mentioned analysis on individual epochs, we also conducted a similar procedure for yearly stacked images with all 170 images. Before stacking, all the images were restored with a common circular Gaussian beam according to observing frequencies: 0.5 mas for the Q band and 1.2 mas for the K band data. The actual distances were 0.7–3.0 mas covered by Q-band data and 1.7–3.0 mas by K-band data. The stacked images have relatively higher signal-to-noise ratios compared with the individual epochs and smooth out the short-term variation, which is better for tracing the yearly variation seen in the M87 jet. Indeed, the analysis from the stacked images reveals the year-scale quasi-sinusoidal evolution of jet PA more clearly, although the trend before 2005 is less definitive owing to the lack of multiple images within each year, in which case a single PA measurement may suffer from short-term temporal fluctuations, as mentioned above. It should also be noted that the evolution of the measured PA at Q and K bands are in good agreement with each other, which indicates the achromatic nature of the observed long-term jet base oscillation. The full sequences of the yearly stacked structure at Q and K bands are shown in Extended Data Figs. 1 and 2, respectively. Note that, in several years, including 2000, 2001, 2002, 2006, 2009, 2011, 2014 and 2015, there are only one or two epochs in those years. Hence, the apparent jet structure is much more knotty than that in other years, the results of which may suffer more uncertainties from the short-term structural variations and data quality compared with data in other observing years.

Precession model

In this section, we describe the precession model and the process of obtaining the relationship between observed data and intrinsic physical

parameters. A sequence of rotation matrices $R_i(\xi)$ are applied to obtain a vector represented in the jet frame to that in the observer frame, where i denotes x, y or z and ξ indicates the anticlockwise rotated angle with respect to the i axis. Observations show that, on average, the jet PA is approximately 288° with a jet (projected) viewing angle of about 17° (ref. 3). The PA variation alone cannot determine the direction of the jet precession. For simplicity, we first assume a clockwise precession with respect to the precession axis. An anticlockwise case fits the data equally well with a suitable shift of the reference time t_0.

In the jet frame, the unit vector of the jet symmetric axis in a Cartesian coordinate system can be expressed as $\mathbf{j} = [0, 0, 1]$. In the precession frame where the precession axis is along the z axis, assuming a precession angular velocity of ω_p, the jet precesses with respect to the z axis with an angle of $\omega_p(t - t_0)$ in a time difference of $(t - t_0)$. The half-opening angle of the jet precession cone is ψ_{jet}. Then the symmetric jet axis represented in the precession frame is obtained by the following operations to $\mathbf{j}$,

$$\mathbf{j}_p = R_z(-\omega_p(t-t_0))R_y(\psi_{jet})\mathbf{j}. \quad (1)$$

In the observer frame, the angle between the precession axis and the z axis (the line of sight) is θ, corresponding to a rotation of $R_y(\theta)$. The projection of the precession axis in the x–y plane makes an angle of η_p with the x axis, corresponding to another rotation of $R_z(\eta_p)$. Therefore, the jet symmetric axis presented in the observer frame can be obtained by applying $R_y(\theta)$ and $R_z(\eta_p)$ successively to that represented in the precession frame, namely,

$$\mathbf{j}_o = R_z(\eta_p)R_y(\theta)\mathbf{j}_p. \quad (2)$$

By combining equation (1) and equation (2), the jet axis components in the observer frame ($j_{xo}(t)$,$j_{yo}(t)$,$j_{zo}(t)$) can be written as

$$j_{xo}(t) = A\cos\eta_p - B\sin\eta_p, \quad (3)$$

$$j_{yo}(t) = A\sin\eta_p + B\cos\eta_p, \quad (4)$$

$$j_{zo}(t) = -\sin(\theta)\cos(-\omega_p(t-t_0))\sin(\psi) + \cos(\theta)\cos(\psi), \quad (5)$$

where,

$$A = \cos(\theta)\cos(-\omega_p(t-t_0))\sin(\psi) + \sin(\theta)\cos(\psi), \quad (6)$$

$$B = \sin(-\omega_p(t-t_0))\sin(\psi). \quad (7)$$

The observed PA $\eta(t)$ is the projected jet axis in the observer frame at observing time point t, which can be expressed as

$$\eta(t) = \arctan\left(\frac{j_{yo}(t)}{j_{xo}(t)}\right). \quad (8)$$

The jet viewing angle at time point t is $\phi(t)$, which can be given by

$$\phi(t) = \arcsin\sqrt{j_{xo}(t)^2 + j_{yo}(t)^2}. \quad (9)$$

There are five free parameters: t_0, η_p, ω_p, ψ_{jet} and θ. The resultant predicted curve of $\eta(t)$ exhibits a quasi-sinusoidal variation with time, with the deviation from a sinusoidal curve depending on the relationship between ψ_{jet} and θ. Namely, there are four situations: (1) when $\theta = 90°$ and $\psi_{jet} < 90°$, the $\eta(t)$ curve is exactly sinusoidal; (2) when $\psi_{jet} < \theta < 90°$ but ψ_{jet} is not close to θ, the $\eta(t)$ curve only slightly deviates from a sinusoid with a small skewness; and (3) when ψ_{jet} is close to but still smaller than θ, a large skewness appears and the direction of the skewness depends on the sense of ω_p; and (4) when $\psi_{jet} > \theta$, the jet rotates around the line of sight as viewed in the two-dimensional projected plane and $\eta(t)$ continuously increases or decreases depending on the sense of ω_p. For the latter two cases, the PA observation would deviate significantly from a sinusoidal curve, and one can then determine all the five parameters in the precession model including the sense of ω_p with the PA observation alone. However, our case has a very small skewness. Since only four parameters are needed to specify a sinusoidal curve and the peak-to-peak amplitude of $\eta(t)$ is determined by both ψ_{jet} and θ, there is a degeneracy between ψ_{jet} and θ when only the PA observation is involved. Also, the sense of ω_p cannot be determined. To break the degeneracy between ψ_{jet} and θ, we include in the fiducial analysis additional constraints of the jet viewing angle which we discuss in the following section.

Note that, although this precession model is based on the solid-body assumption, this assumption eventually loses its validity at larger scales. Moreover, the mass density of M87 jet is low[39,40] and the SMBH in M87 is accreting at sub-Eddington rates[41,42]. In comparison with the sources that have high mass density jets and super-Eddington accretion (that is, SS 433 (ref. 43)), the M87 jet at large scales is significantly more susceptible to the impacts of ambient environment[44].

A Bayesian analysis

We describe here the likelihood function and prior that are used in the Bayesian analysis. According to the Bayes theorem, the posterior reads

$$P(\lambda|q) = \frac{\mathcal{L}(q|\lambda)P(\lambda)}{P(q)}, \quad (10)$$

where $\lambda = (t_0, \eta_p, \omega_p, \psi_{jet}, \theta)$, q stands for observations, $\mathcal{L}(q|\lambda)$ is the (joint) likelihood, $P(\lambda)$ is the prior and $P(\boldsymbol{q})$ is the evidence which only serves as a constant normalization factor. We adopt uniform priors for t_0, η_p, ω_p, ψ_{jet} and θ, as displayed in Extended Data Table 3.

The PA likelihood is assumed to be Gaussian and reads

$$-\ln\mathcal{L}_{PA} = \sum_i \frac{(\eta_p(t_i) - \eta_{ob}(t_i))^2}{2\sigma_i^2}, \quad (11)$$

where σ_i is the uncertainty of the observed PA at t_i. Owing to the poor quality of the VLBA data before 2006, the PAs are the observations from 2006 to 2022 at both 22/24 GHz and 43 GHz.

In addition to the PA observations, we consider the constraints on the jet viewing angle given in the literature. Since the jet is precessing, its viewing angle also varies with time. Therefore, when applying those constraints, we pay attention to the times of the observations. We note that, in the precession model, the angle between the line of sight and precession axis θ is a different physical parameter from that between the line of sight and jet central axis ϕ. Previous studies provided the constraints on ϕ. In ref. 37, a viewing angle of (17.2 ± 3.3)° was reported based on the kinematic analysis with VLBA data observed in 2007, which gives the following Gaussian likelihood (up to a normalization constant)

$$-\ln\mathcal{L}_{VA2007A} = \frac{(\phi_{2007.36} - 17.2)^2}{2\times 3.3^2}, \quad (12)$$

where $\phi_{2007.36}$ is the jet viewing angle at $t = 2007.36$. Furthermore, the brightness ratio of the forward-jet to the counter-jet measured at the distance between 0.4 mas and 0.8 mas from the core from VLBA data gives $(13 \le \phi_{2007.36} \le 27)°$ (ref. 37). We represent this constraint by a piecewise likelihood,

$$-\ln\mathcal{L}_{VA2007B} = \begin{cases} 0, & 13° \le \phi_{2007.36} \le 27°, \\ \infty, & \text{others.} \end{cases} \quad (13)$$

By monitoring the fastest component (6c) with the Hubble Space Telescope from 1994.59 to 1998.55, ref. 45 provided an upper

limit $\phi_{1996.57} \leq 19°$. We represent this constraint by another piecewise likelihood,

$$-\ln\mathcal{L}_{\rm VA1996} = \begin{cases} 0, & \phi_{1996.57} \leq 19°, \\ \infty, & \text{others.} \end{cases} \quad (14)$$

We consider three cases to use the above-mentioned constraints on the jet viewing angle: (1) in Case I, we do not consider additional constraints on the jet viewing angle and use only PA data to perform the analysis; (2) in Case II, we use the uniform distribution $[0, 90]°$ for θ and put constraints on $\phi_{2007.36} = (17.2 \pm 3.3)°$; 3); and (3) in Case III, in addition to Case II we further consider the constraint on $13° \leq \phi_{2007.36} \leq 27°$ and that on $\phi_{1996.57} \leq 19°$. More explicitly,

Case I: $\ln\mathcal{L}(q|\lambda) = \ln\mathcal{L}_{\rm PA}$,

Case II: $\ln\mathcal{L}(q|\lambda) = \ln\mathcal{L}_{\rm PA} + \ln\mathcal{L}_{\rm VA2007A}$,

Case III: $\ln\mathcal{L}(q|\lambda) = \ln\mathcal{L}_{\rm PA} + \ln\mathcal{L}_{\rm VA2007A} + \ln\mathcal{L}_{\rm VA2007B} + \ln\mathcal{L}_{\rm VA1996}$.

We use the Python package EMCEE[46] to explore the five free parameters with an MCMC sampler. We set the walker number to 32 and the iteration number to 10,000.

For these three cases, the marginalized distributions of the parameters are presented in Extended Data Fig. 3a. The results of t_0, $\eta_{\rm p}$ and $\omega_{\rm p}$ are insensitive to the constraints on the jet viewing angle. On the other hand, if only the PA data are used, there is a degeneracy between $\psi_{\rm jet}$ and θ, as shown in Case I in Extended Data Fig. 3. This degeneracy is due to a geometrical effect and, for the same PA variation, the required precession half-opening angle is smaller when the precession axis is more aligned with the line of sight (smaller θ). Such a degeneracy is broken when we apply some prior constraints on the jet viewing angle, which can be seen when we compared Case I with Case II or with Case III. It is worth pointing out that the conclusion of a small jet precession half-opening angle is insensitive to the constraints of ϕ adopted. Indeed, from the amplitude of the PA variation alone, we can already infer that the maximum half-opening angle is $\psi_{\rm jet}^{\rm max} \approx 5°$, which corresponds the case when $\theta = 90°$. Applying the constraints on the jet viewing angle at some specific years further constrains θ and reduces the value of $\psi_{\rm jet}$ to approximately 1°. To break the $\psi_{\rm jet}$–θ degeneracy, we adopt the results obtained from Case III as the final fitting results shown in the main text.

To check the robustness of our final results, we also performed analyses with four different data sets of PA, as shown in Extended Data Fig. 3b. In addition to the data observed from 2006 to 2022 at both Q and K bands applied in Case I to Case III, we consider Cases IV, V and VI, whose likelihoods are the same as Case III except for the different data sets used in $\ln\mathcal{L}_{\rm PA}$. More explicitly, we have, in Case IV, the extended data observed from 2000 to 2022 at both the Q and K bands, in Case V the data observed from 2006 to 2022, but only at the Q band, and in Case VI the extended data observed from 2000 to 2022, but only at the Q band. As shown from the comparison of the parameter constraints through Case III to Case VI, our results are robust whether the poor-quantity data before 2006 are added to the analysis or whether only the data at Q band are being used. The specifications of all cases are listed in Extended Data Table 4 and all the MCMC fitting results are shown in Extended Data Table 5.

To access the goodness-of-fit of our precession model, we define the reduced chi-squared value $\hat{\chi}^2$ as

$$\hat{\chi}^2 = \frac{\ln\mathcal{L}(q|\lambda_{\rm best})}{N_{\rm data} - N_{\rm param}}, \quad (15)$$

where $\boldsymbol{\lambda}_{\rm best}$ is the best-fit model parameter vector, $N_{\rm data}$ is the number of data and $N_{\rm param}$ is the number of model parameters. As shown in Extended Data Table 5, the $\hat{\chi}^2$ values are close to unity for most cases, which indicates that our precession model fits the observations well. Exceptions are Cases IV and VI, where the data before 2006 are included and the $\hat{\chi}^2$ values are larger. However, the increase of the $\hat{\chi}^2$ for these two cases is only caused by one data point at $t = 2000$. If that single data point is excluded from the analysis, the $\hat{\chi}^2$ drops back to around unity, indicating the data point at $t = 2000$ is an outlier. Compared with ref. 36, the derived structure is consistent with previous work. However, the exact reason for the more southern PA with respect to the predicted trend is not very clear at the moment.

GRMHD simulation

We carried out three-dimensional ideal GRMHD simulations of tilted accretion flows and relativistic jets around a spinning BH by using a GR-radiation-MHD code UWABAMI[22]. For simplicity, we ignored the effect of the radiation (that is, radiative force, cooling and so on) for the simulation, as in the aligned disk simulation[23]. We fixed the specific heat index $\gamma_{\rm heat} = 13/9$ because of the combination of the assumption of non-relativistic protons $\gamma_{\rm heat} = 5/3$ and relativistic electrons $\gamma_{\rm heat} = 4/3$. The simulation was carried out up to $3.7 \times 10^4 r_{\rm g}/c$.

The metric can be assumed to be fixed since the accretion rate is too low to affect the space-time geometry. The GRMHD equations in the modified Kerr–Schild coordinate $(r_{\rm sim}, \theta_{\rm sim}, \phi_{\rm sim})$ are integrated. The magnitude of the dimensionless BH spin is set to be $a_* = 0.9375$ (ref. 47), which is close to the value of the maximum spin of a Kerr BH ($|a_*| = 1$|).

We set the initial equilibrium torus with the tilt angle, which is the angle between the BH spin vector and the angular momentum vector of the torus, to be $\theta_{\rm sim} = \psi_{\rm tilt} = 15°$. The direction of the BH spin vector is aligned with the direction of $\theta_{\rm sim} = 0°$. The inner edge $r_{\rm in}$ and the pressure (that is, density) maximum of the initial torus $r_{\rm max}$ were set at $r_{\rm sim} = 20\ r_{\rm g}$ and $33\ r_{\rm g}$, respectively. We note that larger $r_{\rm in}/r_{\rm max}$, which is a sensitive parameter governing the torus size, results in the smaller radius of the outer edge of the initial torus because the weaker pressure gradient force inside the torus is required for the dynamical equilibrium. Here, $r_{\rm in}/r_{\rm max} \approx 0.6$ in our simulation is larger than in a previous work $r_{\rm in}/r_{\rm max} = 0.5$ (ref. 18). As a consequence, the size of the accretion disk $r_{\rm disk}$, which is the average in the disk midplane weighted by rest mass density[18], is initially $r_{\rm disk} \simeq 47\ r_{\rm g}$, that is, a compact initial torus appears in our set-up. A single poloidal magnetic flux loop with a vector potential $A_{\phi_{\rm sim}} \propto \max(\rho/\rho_{\rm max} - 0.2, 0)$ is embedded in the initial torus. Because: (1) the initial torus is relatively compact; (2) it is located at a moderately far radius from the BH; and (3) the initial magnetic field is not as strong in the outer part of the initial torus, and the resultant magnetic flux averaged in time during the precession phase $(1.5–3.7) \times 10^4 r_{\rm g}/c$ at the event horizon is $\phi_{\rm BH} \equiv \Phi_{\rm BH}/\sqrt{\dot{M}_{\rm BH} r_{\rm g}^2 c} \approx 17$, where mass accretion rate is $\dot{M}_{\rm BH} \equiv \int_0^{\pi} {\rm d}\theta_{\rm sim} \int_0^{2\pi} {\rm d}\phi_{\rm sim} \sqrt{-g}\, \rho(r_{\rm sim} = r_{\rm g}, \theta_{\rm sim}, \phi_{\rm sim}) u^{r_{\rm sim}}(r_{\rm sim} = r_{\rm g}, \theta_{\rm sim}, \phi_{\rm sim})$, $\Phi_{\rm BH} \equiv (1/2) \int_0^{\pi} {\rm d}\theta_{\rm sim} \int_0^{2\pi} {\rm d}\phi_{\rm sim} \sqrt{-g}\, B^{r_{\rm sim}}(r_{\rm sim} = r_{\rm g}, \theta_{\rm sim}, \phi_{\rm sim})$. The magnetic field is evaluated and defined in the cgs-Gauss unit. This magnitude of magnetic flux is between the weakly magnetized disk state, so-called SANE (standard and normal evolution, $\phi_{\rm BH} \approx$ few to 10 (refs. 48,49)), and the strongly magnetized disk state, so-called MAD (magnetically arrested disk, $20 \lesssim \phi_{\rm BH} \lesssim 60$ (refs. 50,51)), and, therefore, this intermediate state that we adopted is sometimes called semi-MAD[52,53].

The inner and outer boundaries of the simulation domain are set to be $r_{\rm in} = 1.18\ r_{\rm g}$ and $r_{\rm out} = 10\ r_{\rm g}$. The simulation domain is divided into $(N_{r_{\rm sim}}, N_{\theta_{\rm sim}}, N_{\phi_{\rm sim}}) = (200, 144, 96)$ meshes in the $r_{\rm sim}$, $\theta_{\rm sim}$ and the $\phi_{\rm sim}$ directions, respectively. As in most of the works on GRMHD simulations of accretion flows, the interval of radial grid points exponentially increases with radius and the grid points in the $\theta_{\rm sim}$ direction concentrates near the equatorial plane of the coordinate system[54]. Because the initial magnetic field is amplified by means of the magneto-rotational instability (MRI[55]), the spatial resolution of the simulation domain can affect the resulting magnetic field strength. The MRI quantity factor (Q-factor), which evaluates the number of available meshes to resolve

the fastest growing mode of MRI[49,56], is $(Q^{r_{\rm sim}}, Q^{\theta_{\rm sim}}, Q^{\phi_{\rm sim}}) \simeq (8.1, 4.9, 18)$. Here, to evaluate the Q-factors, we analysed the same region as in previous work on non-tilted accretion flows[49], except that we extended the region by ±15° in the $\theta_{\rm sim}$ direction, that is, $45° \le \theta_{\rm sim} \le 135°$, to take into account the precession of the disk with initial tilt angle 15°. The resulting Q-factors are smaller than the required values suggested in a previous work[56] ($Q^z \approx 10$ and $Q^{\phi_{\rm sim}} \approx 20$, in the cylindrical coordinates); however, they satisfy the ones proposed by another previous work[57] ($Q \approx 6$ in the Cartesian coordinates). Therefore, this simulation would marginally resolve the growth of MRI.

For the analysis of the tilt and precession angles, we follow a process similar to that described in a previous work[16]. We evaluated the tilt angle $\psi_{\rm tilt}$ and the precession angle $\phi_{\rm prec}(r_{\rm sim})$ at a certain radius as follows.

$$\Psi_{\rm tilt}(r_{\rm sim}) = \arccos\left(\frac{\mathbf{J}_{\rm BH}\cdot\mathbf{J}_{\rm MHD}(r_{\rm sim})}{|\mathbf{J}_{\rm BH}||\mathbf{J}_{\rm MHD}(r_{\rm sim})|}\right), \tag{16}$$

$$\phi_{\rm prec}(r_{\rm sim}) = \arccos\left(\frac{\mathbf{J}_{\rm BH}\times\mathbf{J}_{\rm MHD}(r_{\rm sim})}{|\mathbf{J}_{\rm BH}\times\mathbf{J}_{\rm MHD}(r_{\rm sim})|}\cdot\mathbf{e}_y\right), \tag{17}$$

where $\mathbf{e}_y$ is the unit vector along the y axis, $\mathbf{J}_{\rm BH}$ is the dimensionless angular momentum vector of the BH and $\mathbf{J}_{\rm MHD}$ is the angular momentum of the MHD plasma in an asymptotically flat space.

$$\mathbf{J}_{\rm BH} = a_*\mathbf{e}_z, \tag{18}$$

$$\mathbf{J}_{\rm MHD} = J^x_{\rm MHD}\mathbf{e}_x + J^y_{\rm MHD}\mathbf{e}_y + J^z_{\rm MHD}\mathbf{e}_z. \tag{19}$$

We define $J^i_{\rm MHD}\,(i = x, y, z)$ as

$$(J_{\rm MHD})_\delta = \frac{\epsilon_{\alpha\beta\gamma\delta}L^{\alpha\beta}P^\gamma}{2\sqrt{P^\mu P_\mu}}, \tag{20}$$

where $L^{\alpha\beta}$ and $P^\gamma(r_{\rm sim})$ are the total angular momentum and total four-momentum inside the shell of the width Δr, respectively, which are described as

$$L^{\alpha\beta}(r_{\rm sim}) = \int (x^\alpha T^{\beta 0} - x^\beta T^{\alpha 0})\mathrm{d}^3x, \tag{21}$$

$$P^\gamma(r_{\rm sim}) = \int T^{\gamma 0}\mathrm{d}^3x. \tag{22}$$

It is useful to note that $P^\gamma(r_{\rm sim})/\sqrt{P^\mu(r_{\rm sim})P_\mu(r_{\rm sim})}$ is the four-velocity of the mass centre.

It should be noted that, in our simulation, an LT precession of the accretion disk occurs with an almost constant precession period after the system evolves into a steadily precessing state, which is in agreement with ref. 19. For their $a_* = 0.9$ case, the precession rate is approximately 4° per 1,000 $r_{\rm g}/c$, which corresponds to a period of $T \approx 90$ years after adopting the M87 BH mass. The shorter period in our case (that is, $T \approx 11$ years, which matches the inferred period from observation) would be attributed to the final disk size, higher magnitude of BH spin $a_* = 0.9375$ and/or our larger specific heat ratio 13/9, which will result in the rapid wave propagation in the disk for the rigid-body precession[24]. As mentioned above, our simulation marginally resolves MRI. Regarding this, ref. 18 raises the caution that if MRI is sufficiently resolved, the disk would expand and the precession would be slowed down. However, the consistency between our simulation and that with a higher resolution performed in ref. 19 somehow justifies our simulated result. Although there may still be uncertainties regarding whether the simulation time is long enough, a smaller disk would be a preferred set-up for obtaining the inferred period from the observations. Indeed, since the M87 disk size is so far poorly constrained, one may adjust the initial disk size to compensate for the disk expansion if the simulation is really under-resolved. Nonetheless, systematic works are warranted to explore broader parameter space and other physical properties in tilted systems, such as the feeding of an outer disk and the magnetic field morphology. Our observation of the jet precessing provides important information and constraints for numerical studies of tilted-disk systems, in particular, for M87.

Alternative origins of the variations in jet position angle

Here, we discuss the alternative scenarios which could cause the jet PA variations, including binary BH (BBH) systems, instabilities and disk-jet interactions.

In the BBH system, a precessing jet is developed if the primary BH has an accretion disk that is not co-planar with the binary system orbit. The disk is forced to precess by the effect of the torque from the secondary BH[58,59]. This situation is similar to a tilted-disk system. The formed jet from the primary BH will precess as seen in tilted-disk simulations. However, we do not have any observational evidence of a BBH system in M87. One of the best candidates for the SMBH system OJ287 has presented quasi-periodic double-peaked optical outbursts that have been interpreted as being produced by a secondary BH impacting twice the accretion disk of the primary. In M87, such quasi-periodic outbursts have not been observed yet. If the M87 is a BBH system, we may see the position change of the radio core of the M87. However, from our long-term radio monitoring of the radio core of M87, we do not see such evidence. The horizon-scale images of M87 by the Event Horizon Telescope observation have not shown any structure by a secondary BH. From the observational evidence, we think that the BBH scenario is not preferred.

In the instabilities, we have a possibility to grow two major types, Kelvin–Helmholtz and current-driven kink instabilities during jet propagation. Kelvin–Helmholtz instability is excited by the velocity shear which naturally happens at the boundary between the jet and the external medium. A helical mode of KH instability will develop a helical structure inside the jet. However, the existence of a strong magnetic field suppresses the growth of Kelvin–Helmholtz instability[13]. Our observed jet region is located in the jet acceleration and collimation zone. From the jet formation mechanism by the MHD process, in such a region, the magnetic field is dominant. Thus, Kelvin–Helmholtz instability is not suitable for the origin of the precessing jet of M87. Instead of KH instability, current-driven kink instability will grow in the jet, which is excited by the existence of a helical magnetic field. A helical magnetic field is naturally expected from GRMHD simulations of jet formation[49,60]. Current-driven kink instability has faster growth in a strongly magnetized region and a developed helically twisted jet structure. The helically twisted structure is advected along the jet while expanding radially[61,62]. The growth rate of the current-driven kink instability depends on the magnetic pitch (the ratio of poloidal and toroidal magnetic field) and local Alfven speed (that is, magnetic field strength). In general, the growth rate of the current-driven kink instability varies with jet radius. However, such a feature of varying amplitude at different locations is not apparent within our selected regions, as viewed from Fig. 1 and from the consistency between the variation amplitudes obtained from two analyses using different jet distance ranges, namely, 0.7–3.0 mas versus 1.7–3.0 mas from the core. Thus, the current-driven kink instability scenario is also disfavoured.

In the disk-jet interaction scenario, the jet structure is affected by the inhomogeneous mass accretion onto a BH (mass injection to the jet). In the MAD phase, mass accretion onto a BH is stopped locally by strong magnetic pressure[50]. Disruption of accretion flows will have a certain period. It would be possible to make a quasi-period mass accretion. However, the timescale is roughly several 1,000 $r_{\rm g}/c$ which is shorter than the observed period. Such local disruption of accretion flows will trigger the excitement of instabilities and produce an asymmetric structure in the jet. They would be the same as the instability scenario.

Data availability

The raw data can be downloaded from the EAVN Archive system (https://radio.kasi.re.kr/arch/search.php) and NRAO Archive Interface (https://data.nrao.edu/portal/#/). The calibrated data used in this paper are available from the corresponding author upon reasonable request due to the ongoing projects. Source data are provided with this paper.

Code availability

For data processing, we utilize public software, including AIPS for calibration (http://www.aips.nrao.edu/index.shtml), DIFMAP for imaging (https://sites.astro.caltech.edu/~tjp/citvlb/) and Python package EMCEE for MCMC fitting (https://pypi.org/project/emcee/). The codes for the simulations in this paper are available from the corresponding author upon reasonable request due to the ongoing and follow-up projects.

31. Cui, Y. Z. & Hada K. *Amplitude Calibration Guideline of TMRT and NSRT* (EAVN Data Reduction Guideline, 2020).
32. Greisen, E. W. in *Information Handling in Astronomy – Historical Vistas* (ed. Heck, A.) Vol. 285, 109–125 (Kluwer Academic Publishers, 2003).
33. Högbom, J. A. Aperture synthesis with a non-regular distribution of interferometer baselines. *Astron. Astrophys. Suppl. Ser.* **15**, 417–426 (1974).
34. Shepherd, M. C., Pearson, T. J. & Taylor, G. B. DIFMAP: an interactive program for synthesis imaging. *Bull. Am. Astron. Soc.* **26**, 987–989 (1994).
35. Ly, C., Walker, R. C. & Wrobel, J. M. An attempt to probe the radio jet collimation regions in NGC 4278, NGC 4374 (M84), and NGC 6166. *Astron. J.* **127**, 119–124 (2004).
36. Ly, C., Walker, R. C. & Junor, W. High-frequency VLBI imaging of the jet base of M87. *Astrophys. J.* **660**, 200–205 (2007).
37. Mertens, F., Lobanov, A. P., Walker, R. C. & Hardee, P. E. Kinematics of the jet in M 87 on scales of 100–1000 Schwarzschild radii. *Astron. Astrophys.* **595**, A54 (2016).
38. Hada, K. The structure and propagation of the misaligned jet M87. *Galaxies* **5**, 2 (2017).
39. Ferrari, A. Modeling extragalactic jets. *Annu. Rev. Astron. Astrophys.* **36**, 539–598 (1998).
40. Kino, M. & Takahara, F. Constraints on the energetics and plasma composition of relativistic jets in FR II sources. *Mon. Not. R. Astron. Soc.* **349**, 336–346 (2004).
41. Narayan, R., Yi, I. & Mahadevan, R. Explaining the spectrum of Sagittarius A* with a model of an accreting black hole. *Nature* **374**, 623–625 (1995).
42. Chatterjee, K. & Narayan, R. Flux eruption events drive angular momentum transport in magnetically arrested accretion flows. *Astrophys. J.* **941**, 30 (2022).
43. Hjellming, R. M. & Johnston, K. J. An analysis of the proper motions of SS 433 radio jets. *Astrophys. J. Lett.* **246**, L141–L145 (1981).
44. McKinney, J. C. General relativistic magnetohydrodynamic simulations of the jet formation and large-scale propagation from black hole accretion systems. *Mon. Not. R. Astron. Soc.* **368**, 1561–1582 (2006).
45. Biretta, J. A., Sparks, W. B. & Macchetto, F. Hubble Space Telescope observations of superluminal motion in the M87 jet. *Astrophys. J.* **520**, 621–626 (1999).
46. Foreman-Mackey, D., Hogg, D. W., Lang, D. & Goodman, J. emcee: the MCMC hammer. *Publ. Astron. Soc. Pac.* **125**, 306–312 (2013).
47. Gammie, C. F., Shapiro, S. L. & McKinney, J. C. Black hole spin evolution. *Astrophys. J.* **602**, 312–319 (2004).
48. Narayan, R., SÄ dowski, A., Penna, R. F. & Kulkarni, A. K. GRMHD simulations of magnetized advection-dominated accretion on a non-spinning black hole: role of outflows. *Mon. Not. R. Astron. Soc.* **426**, 3241–3259 (2012).
49. Porth, O. et al. The Event Horizon general relativistic magnetohydrodynamic code comparison project. *Astrophys. J. Suppl. Ser.* **243**, 26 (2019).
50. Tchekhovskoy, A., Narayan, R. & McKinney, J. C. Efficient generation of jets from magnetically arrested accretion on a rapidly spinning black hole. *Mon. Not. R. Astron. Soc.* **418**, L79–L83 (2011).
51. Narayan, R., Chael, A., Chatterjee, K., Ricarte, A. & Curd, B. Jets in magnetically arrested hot accretion flows: geometry, power, and black hole spin-down. *Mon. Not. R. Astron. Soc.* **511**, 3795–3813 (2022).
52. White, C. J., Quataert, E. & Gammie, C. F. The structure of radiatively inefficient black hole accretion flows. *Astrophys. J.* **891**, 63 (2020).
53. Anantua, R., Ressler, S. & Quataert, E. On the comparison of AGN with GRMHD simulations: I. Sgr A*. *Mon. Not. R. Astron. Soc.* **493**, 1404–1418 (2020).
54. Gammie, C. F., McKinney, J. C. & Tóth, G. HARM: a numerical scheme for general relativistic magnetohydrodynamics. *Astrophys. J.* **589**, 444–457 (2003).
55. Balbus, S. A. & Hawley, J. F. A powerful local shear instability in weakly magnetized disks. I. Linear analysis. *Astrophys. J.* **376**, 214 (1991).
56. Hawley, J. F., Guan, X. & Krolik, J. H. Assessing quantitative results in accretion simulations: from local to global. *Astrophys. J.* **738**, 84 (2011).
57. Sano, T., Inutsuka, S. I., Turner, N. J. & Stone, J. M. Angular momentum transport by magnetohydrodynamic turbulence in accretion disks: gas pressure dependence of the saturation level of the magnetorotational instability. *Astrophys. J.* **605**, 321–339 (2004).
58. Abraham, Z. Jet precession in binary black holes. *Nat. Astron.* **2**, 443–444 (2018).
59. Britzen, S. et al. OJ287: deciphering the 'Rosetta stone of blazars'. *Mon. Not. R. Astron. Soc.* **478**, 3199–3219 (2018).
60. Cruz-Osorio, A. et al. State-of-the-art energetic and morphological modelling of the launching site of the M87 jet. *Nat. Astron.* **6**, 103–108 (2022).
61. Mizuno, Y., Hardee, P. E. & Nishikawa, K. I. Spatial growth of the current-driven instability in relativistic jets. *Astrophys. J.* **784**, 167 (2014).
62. Singh, C. B., Mizuno, Y. & de Gouveia Dal Pino, E. M. Spatial growth of current-driven instability in relativistic rotating jets and the search for magnetic reconnection. *Astrophys. J.* **824**, 48 (2016).

Acknowledgements We thank W. Wang, C. Yim, Z. Wang, F. Gu, Y. Feng, M. Nakamura, S. Zhao and T. Yanagida for discussions and their support. This project is funded by the China Postdoctoral Science Foundation (grant no. 2022M712084) and the Key Research Project of Zhejiang Lab no. 2021PE0AC03. Y.C. is supported by the Japanese Government (MEXT) Scholarship. This work is partially supported by the MEXT/JSPS KAKENHI (grant nos. JP18H03721, JP19H01943, JP18KK0090, JP2101137, JP21H04488, JP22H00157, JP18K13594, JP19H01908, JP19H01906, JP18K03656, JP19KK0081). This work has been supported by the National Key R&D Program of China (grant no. 2022YFA1603104), the Major Program of the National Natural Science Foundation of China (grant nos. 11590780, 11590784) and the Key Research Program of Frontier Sciences, CAS (grant no. QYZDJ-SSW-SLH057). T.K. is supported in part by MEXT SPIRE, MEXT as 'Priority Issue on post-K computer' (Elucidation of the Fundamental Laws and Evolution of the Universe) and as 'Program for Promoting Researches on the Supercomputer Fugaku' (Toward a unified view of the universe: from large scale structures to planets and Structure and Evolution of the Universe Unraveled by Fusion of Simulation and AI; grant no. JPMXP1020230406) and JICFuS. The GRMHD simulations were carried out on the XC50 at the Center for Computational Astrophysics, National Astronomical Observatory of Japan. Y.M. is supported by the National Natural Science Foundation of China (grant no. 12273022) and the Shanghai pilot programme of international scientists for basic research (grant no. 22JC1410600). J.Y.K. acknowledges the support from the National Research Foundation of Korea (grant no. 2022R1C1C1005255). S.T. acknowledges financial support from the National Research Foundation of Korea (NRF) grant no. 2022R1F1A1075115. This research was supported by the Korea Astronomy and Space Science Institute under the R&D program supervised by the Ministry of Science and ICT. H.R. and B.W.S. acknowledge support from the KASI-Yonsei DRC program of the Korea Research Council of Fundamental Science and Technology (DRC-12-2-KASI). I.C. acknowledges financial support in part by the Consejería de Economía, Conocimiento, Empresas y Universidad of the Junta de Andalucía (grant no. P18-FR-1769), the Consejo Superior de Investigaciones Científicas (grant no. 2019AEP112), and the Severo Ochoa grant no. CEX2021-001131-S funded by MCIN/AEI/ 10.13039/501100011033. R.-S.L. is supported by the Key Program of the National Natural Science Foundation of China (grant no. 11933007); the Key Research Program of Frontier Sciences, CAS (grant no. ZDBS-LY-SLH011); the Shanghai Pilot Program for Basic Research, Chinese Academy of Sciences, Shanghai Branch (JCYJ-SHFY-2022-013) and the Max Planck Partner Group of the MPG and the CAS. This work made use of the East Asian VLBI Network (EAVN), which is operated under cooperative agreement by the National Astronomical Observatory of Japan (NAOJ), Korea Astronomy and Space Science Institute (KASI), Shanghai Astronomical Observatory (SHAO), Xinjiang Astronomical Observatory (XAO), Yunnan Observatories (YNAO), National Astronomical Research Institute of Thailand (Public Organization) (NARIT), and National Geographic Information Institute (NGII), with the operational support by Ibaraki University (for the operation of Hitachi 32 m and Takahagi 32 m), Yamaguchi University (for the operation of Yamaguchi 32 m) and Kagoshima University (for the operation of VERA Iriki antenna). The Nanshan 26 m radio telescope (NSRT) is operated by the Urumqi Nanshan Astronomy and Deep Space Exploration Observation and Research Station of Xinjiang. The Sardinia Radio Telescope is funded by the Ministry of University and Research (MIUR), Italian Space Agency (ASI), and the Autonomous Region of Sardinia (RAS) and is operated as National Facility by the National Institute for Astrophysics (INAF). The Medicina radio telescope is funded by the MIUR and is operated as a National Facility by the INAF. The VLBA is an instrument of the National Radio Astronomy Observatory. The National Radio Astronomy Observatory is a facility of the National Science Foundation operated by Associated Universities, Inc.

Author contributions Y.C. led the project. Y.C., K.H., H.R., K.Y., Jintao Yu, J.P., W.J. and E.K. worked on the data calibration, image reconstruction, analysis and interpretation of the results. T.K., M.K., W.L., Y.M., M.H. and Z.S. worked on the theoretical implications, simulations and interpretation of the results. Y.C. wrote the original manuscript. J.-C.A., X.C., I.C., G.G., M.G., T.J., R.-S.L., K.N., J.O., K.O., S.S.-S., B.W.S., H.T., M.T., F.T., S.T. and K.W. contributed to the scientific discussions by means of the EAVN Active Galactic Nuclei Science Working Group's regular meetings. Kazunori Akiyama, T.A., Keiichi Asada, S.B., D.B., L.C., Y.H., T.H., J.H., N.K., J.-Y.K., S.-S.L., J.W.L., J.A.L., G.M., A. Melis, A. Melnikov, C.M., S.-J.O., K.S., X.W., Y.Z., Z.C., J.-Y.H., D.-K.J., H.-R.K., J.-S.K., H.K., B.L., G.L., Xiaofei Li, Z.L., Q.L., Xiang Liu, C.-S.O., T.O., D.-G.R., J.W., N.W., S.W., B.X., H.Y., J.-H.Y., Y.Y., Jianping Yuan, H.Z., R.Z. and W.Z. conducted observations and worked on data correlation and antenna maintenance. All authors contributed to the discussion of the results presented and commented on the manuscript.

Competing interests The authors declare no competing interests.

Additional information

Supplementary information The online version contains supplementary material available at https://doi.org/10.1038/s41586-023-06479-6.

Correspondence and requests for materials should be addressed to Yuzhu Cui.

Peer review information *Nature* thanks James Moran and the other, anonymous, reviewer(s) for their contribution to the peer review of this work. Peer reviewer reports are available.

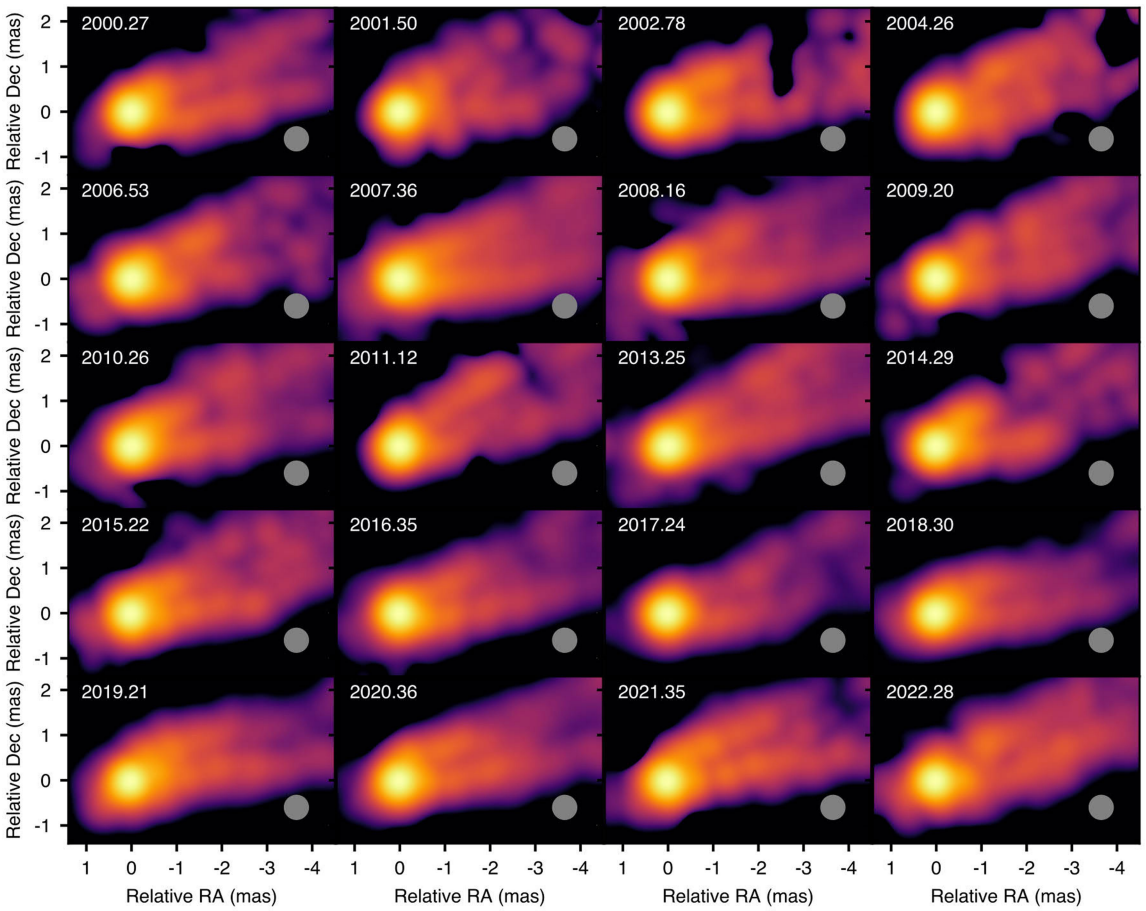

Extended Data Fig. 1 | Structural evolution of M87 jet 2000–2022 at Q band. The images are produced by the yearly stacked EAVN and VLBA data. A common circular restoring beam with FWHM of 0.5 mas (shown in the bottom-right corner of each panel) is used for all individual images before stacking. The observing year is indicated at the top-left corner.

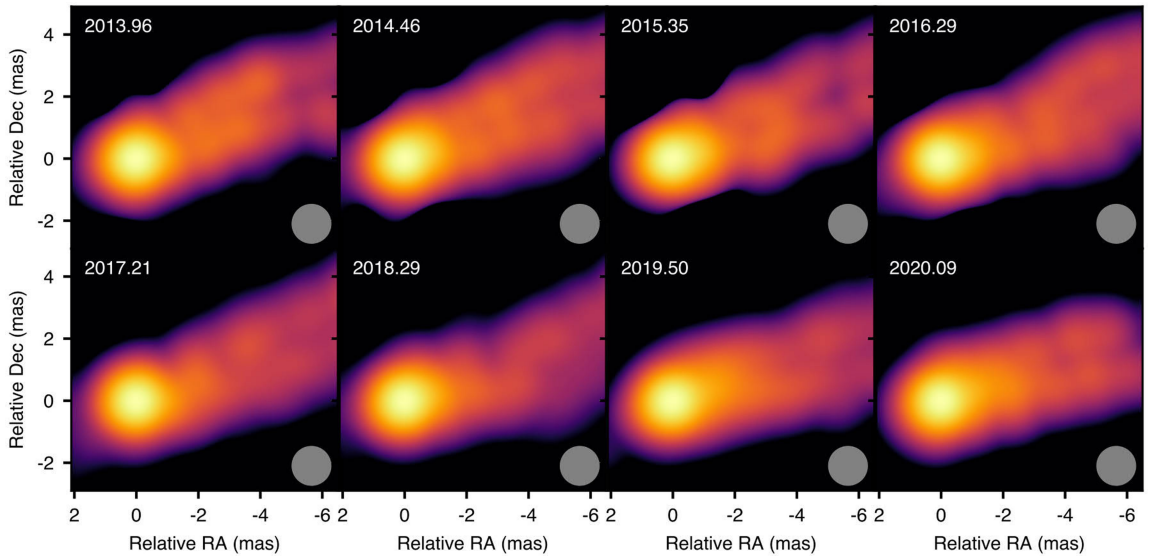

Extended Data Fig. 2 | Structural evolution of M87 jet 2013–2020 at K band. The images are produced by the yearly stacked EAVN and VLBA data. A common circular restoring beam with FWHM of 1.2 mas (shown in the bottom-right corner of each panel) is used for all individual images before stacking. The observing year is indicated at the top-left corner.

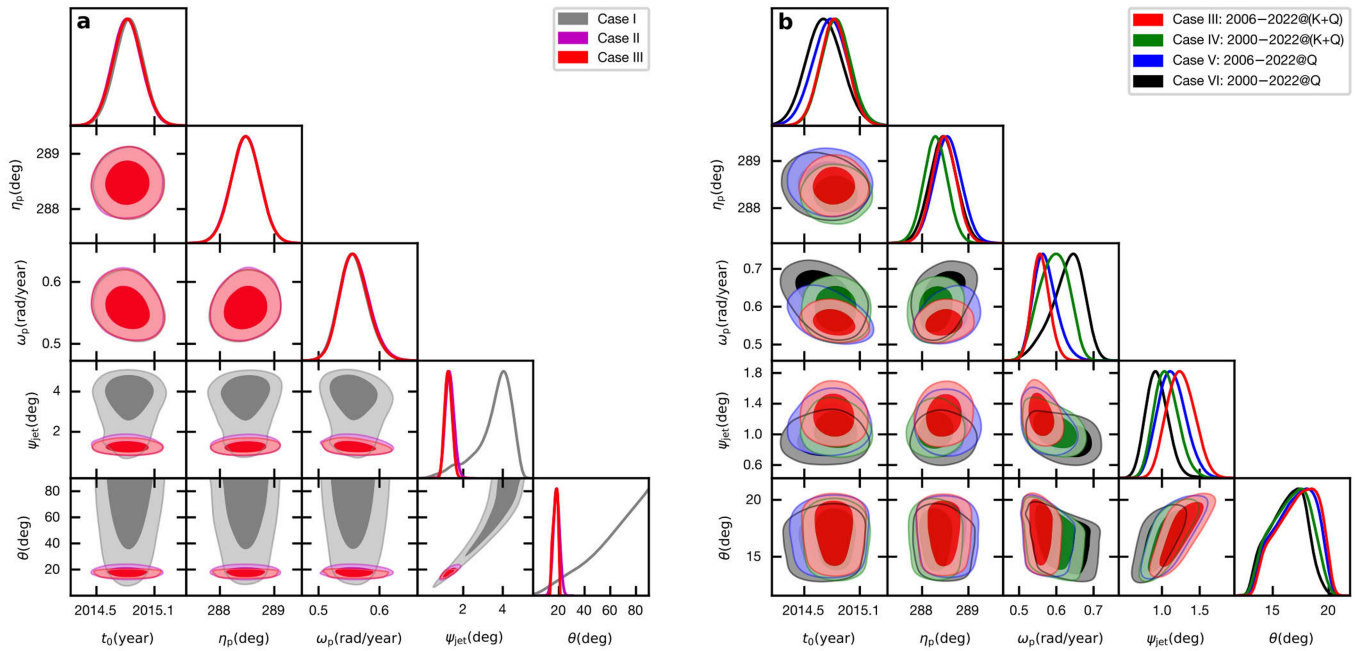

Extended Data Fig. 3 | Posterior distributions of precession model parameters in different cases. (a): comparison among Case I–III with different constraints. **(b)**: comparison among Case III–VI with different data sets. The detailed information for each case is described in Extended Data Table 4 and Methods. The contours correspond to the 68% and 95% confidence levels.

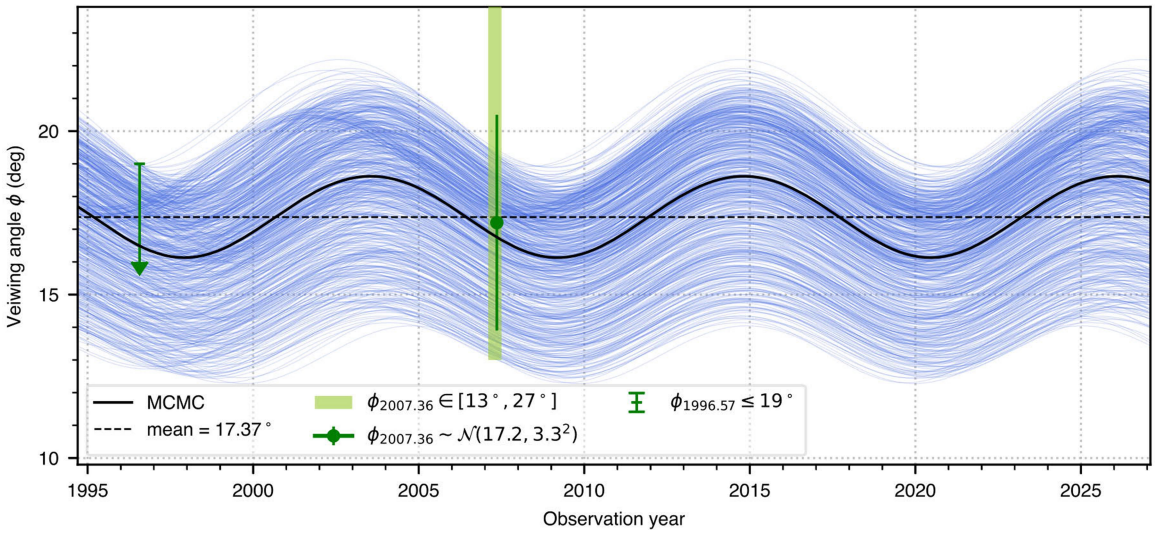

Extended Data Fig. 4 | Evolution of the viewing angle ϕ as a function of time. The black thick line is derived from the best-fit precession model parameters. The blue thin lines are plotted by the randomly chosen model parameters derived from the MCMC samples and represent the statistical errors. The constraint of $\phi_{2007.36} \sim \mathcal{N}(17.2, 3.3^2)$ obtained from ref. 37 is represented by the green dot with an error bar of one standard deviation. The constraints of $\phi_{1996.57} \leq 19°$[45] and $\phi_{2007.36} \in [13, 27]°$[37] are indicated with green arrow and shadow, respectively.

Extended Data Table 1 | Summary of the data from the different arrays

Array	Frequency (GHz)	Θ^a (mas)	$N^b_{\rm epoch}$	$Y^c_{\rm ob}$
EAVN[d]	22/43	0.55/0.63	119	2013–2021
VLBA	24/43	0.40/0.23	47	2006–2018
EATING	22	0.27	4	2017, 2019, 2020

[a]Typical angular resolution. [b]Number of the epochs. [c]Observing years. [d]Part of EAVN observations were conducted with only the KaVA array. The angular resolution of only KaVA is 1.26 mas at 22 GHz and 0.63 mas at 43 GHz.

Extended Data Table 2 | Antenna information of four EATING observations at 22 GHz

Epoch	Obs. Date	$N^{a}_{\rm Ant}$	Stations
a17107a	2017-04-17	11	KaVA[b] (no KUS), TMRT[c], NSRT[d], HIT[e], MDC[f]
a19mk02q	2019-12-06	9	KaVA, NSRT, SRT[g]
a19mk02r	2019-12-21	9	KaVA, NSRT, BDR[h]
a2015a	2020-01-30	8	KaVA, SRT

[a]Number of participated antenna. [b]KaVA: Korean VLBI Network (KVN) and VERA, including Mizusawa-20m, Iriki-20m, Ishigaki-20m, Ogasawara-20m telescopes in Japan and Tamna-21m, Ulsan-21m, Yonsei-21m telescopes in Korea. [c]Tianma-65m telescope in China. [d]Nanshan-26m telescope in China. [e]Hitachi-32m telescope in Japan. [f]Medicina-32m telescope in Italy. [g]Sardinia-64m telescope in Italy. [h]Badary-32m telescope in Russia.

Extended Data Table 3 | Common prior distribution for each parameter in Case I–Case VI

Parameter	Type	Details	Unit
t_0	Uniform	[2012, 2018]	year
$\eta_{\rm p}$	Uniform	[280, 295]	deg
$\omega_{\rm p}$	Uniform	[0, 1]	radian/year
$\psi_{\rm jet}$	Uniform	[0, 5]	deg
θ	Uniform	[0, 90]	deg

The specifications for different cases are listed in Extended Data Table 4.

Extended Data Table 4 | Detailed specifications for Case I–Case VI

Label	Data	Additional constraints
Case I	2006–2022 at K and Q bands	no additional constraints
Case II	same as above	$\phi_{2007.36} \sim \mathcal{N}(17.2, 3.3^2)$ [37]
Case III	same as above	$\phi_{2007.36} \sim \mathcal{N}(17.2, 3.3^2)$, $\phi_{2007.36} \in [13, 27]^\circ$ [37], $\phi_{1996.57} \leq 19^\circ$ [45]
Case IV	2000–2022 at K and Q bands	same as above
Case V	2006–2022 at Q band	same as above
Case VI	2000–2022 at Q band	same as above

$\phi_{2007.36} \sim \mathcal{N}(17.2, 3.3^2)$ indicates the Gaussian distribution for ϕ at t=2007.36 years based on ref. 37. The corresponding MCMC fitting results are compared in Extended Data Fig. 3 and listed in Extended Data Table 5.

Extended Data Table 5 | MCMC fitting results for Case I–Case VI

	t_0	$\eta_{\rm p}$ (°)	$\omega_{\rm p}$ (radian/year)	$\psi_{\rm jet}$ (°)	θ (°)	$T_{\rm prec}^{\rm jet}$(year)	$\hat{\chi}^2$
Case I	2014.84 ± 0.15	288.47 ± 0.27	0.56 ± 0.02	3.56 ± 0.93	62.71 ± 20.54	11.27 ± 0.48	N/A[a]
Case II	2014.82 ± 0.15	288.47 ± 0.26	0.56 ± 0.02	1.32 ± 0.22	18.14 ± 2.40	11.22 ± 0.48	1.25
Case III	2014.82 ± 0.15	288.47 ± 0.27	0.56 ± 0.02	1.25 ± 0.18	17.21 ± 1.74	11.24 ± 0.47	1.25
Case IV	2014.84 ± 0.16	288.29 ± 0.26	0.59 ± 0.04	1.06 ± 0.16	16.63 ± 1.68	10.58 ± 0.68	1.98
Case V	2014.78 ± 0.19	288.55 ± 0.30	0.57 ± 0.03	1.13 ± 0.18	17.01 ± 1.73	11.01 ± 0.61	1.53
Case VI	2014.72 ± 0.19	288.45 ± 0.30	0.63 ± 0.04	0.94 ± 0.15	16.31 ± 1.57	9.99 ± 0.70	2.32

The last column is the reduced χ^2 value calculated with the best-fit model parameters (see Equation (15)). We adopt Case III as the final fitting results as shown in Table 1. [a]For Case I, χ^2 is not applicable since there is a degeneracy between $\psi_{\rm jet}$ and θ. The values correspond to the means of the MCMC samples with standard deviations.

Extended Data Table 6 | Jet viewing angle at some selected years

Year	2017	2018	2019	2020	2021	2022	2023
ϕ (deg)	17.7 ± 1.8	17.0 ± 1.7	16.4 ± 1.7	16.0 ± 1.6	16.0 ± 1.6	16.4 ± 1.6	17.0 ± 1.7

Errors are standard deviations.